University of Thi-Qar Journal of Science (UTJsci)
E-ISSN: 2709-0256, P-ISSN: 1991-8690, Vol. 11, No. 1, Jun. 2024

A Plasmonic Photonic Crystal Fiber Sensor with Simplified Features for Identifying Unidentified Analytes

Hassan A. Yasser*[1a] and Mostefa Benhalilibа[2b]

[1] *Department of Physics, College of Science, University of Thi-Qar, Thi-Qar, Iraq.*
[2] *FDFCA Research Group USTOMB, 31130 Oran, Algeria.*
[b]mostefa.benhalilibа@univ-usto.dz
*[a] Corresponding author: hassan.yasser_ph@sci.utq.edu.iq

Received: 2024-02-22, Revised: 2024-03-18, Accepted: 2024-03-20, Published: 2024-06-01

***Abstract*— In this paper, we present a novel method for building a plasmonic photonic crystal fiber (PCF) sensor with simplified features to identify unknown analytes. Using the special parameters of plasmonic PCFs, the suggested sensor increases the sensitivity and specificity of target analyte detection. We provide a streamlined design approach that reduces manufacturing complexity without sacrificing reliable performance, opening up the sensor to new useful applications. We show the optimal structure parameters for optimizing sensitivity using the finite element method in the COMSOL environment. The suggested configuration attained strong spectral sensitivity throughout an extensive range of the analyte's refractive indices. Furthermore, a perfect linear connection was established between the analyte's refractive index and the resonant wavelength, qualifying the sensor for usage across the whole range of the analyte's refractive indices.**

***Keywords*— plasmonic, PCF, sensitivity of sensor.**

I. INTRODUCTION

Because of its numerous uses, plasmonic photonic crystal fiber (PCF) sensorswhich are highly sensitive and selective,have witnessed tremendous advancements in recent years. These sensors improve light-matter interaction and sensing capabilities using plasmonic materials and PCF structure [1,2]. Plasmon-coupled force field sensors aim to detect analytes or environmental changes with high sensitivity and selectivity, benefiting industries like environmental monitoring and biological diagnostics [3,4]. The label-free monitoring and real-time analyte detection capabilities of PCF-based surface plasmon resonance (SPR) sensors have drawn attention [5]. Gold is a common choice for plasmonic materials in these sensors, where the issue is the proper selection and modification of PCF design parameters for enhanced sensing performance and detection range [6-8]. Overall, SPR-based PCF sensors offer greater sensitivity and precision in detecting various analytes, making them valuable tools in research and technology fields [9]. Particularly because of its exceptional label-free monitoring and real-time analyte detection capabilities, SPR sensors based on PCF have garnered a lot of interest [10–12]. The free electrons on the metal surface have the ability to absorb incident light. As a result, a surface plasmon wave (SPW) is produced [13]. When stimulated at the SPR wavelength, the conspicuous loss peak shows extremely great sensitivity to the liquid analytes [14]. When the PCF's phase-matching requirement between the fundamental and surface plasmon-polariton (SPP) modes is met, the SPR is frequently employed in optical fiber detection [15]. To advance PCF sensing technology, several SPR-based PCF refractive index sensor types have been investigated within the last 20 years [12–18]. The detection of biological and biomolecular analytes [4], bioengineering [9], biochemistry [6], and bioimaging [17] are only a few applications for the SPR phenomenon. The literature has provided a variety of PCF-SPR sensor designs, such as D-shaped configurations [14], slotted topologies [19], and internal and external metal coating [20]. Due to their unusually high refractive indices (RI), liquids with lower RI values are difficult for optical fibers to distinguish from one another [21]. PCF sensors can help with this issue. Because of their distinct periodic air-hole cladding structure, they can lower the core's refractive index and make detection easier [22]. Since the evanescent wave of the light matches the wave vector of the plasma wave on the metal surface, resonance happens when light incidence occurs on a metal surface [23]. The most of the energy carried by the incident light is now absorbed by the surface plasma wave, which also lowers the energy of the reflected light. When used to optical sensors, SPR is based on the physics previously mentioned [24]. On the other hand, light typically has a lower wavevector than metal plasma. Therefore, it is essential to match the two waves that reach the wavevector when utilizing a unique PCF structure [25].

In this work, we examined a plasmonic PCF sensor constructed using the finite element method (FEM) in the COMSOL environment. We employ a metal film that is a part of the PCF framework. Our design positions the gold surface at a distance from the sample under evaluation. Part of the optical fiber's periphery is covered in gold. The excited SPPs in the gold produce absorption. When a PCF-guided mode resonates with the SPP, the absorption

https://doi.org/10.32792/utq/utjsci/v11i1.1176

increases. The mode and SPP's phase-matching need to be met for this to happen. The sensor can detect minute changes in the refractive index of the sample over a broad wavelength range. We also explore the possibility of improving the sensitivity by adjusting sensor parameters.

Many sensors are available in scientific research, and each of them has limitations that may relate to the range of the refractive index of the analyte or the sensitivity achieved. The proposed sensor is characterized by the fact that it operates over a wide range of analyte refractive indices and achieves spectral sensitivity and acceptable analysis.

II. SENSOR DESIGN

The proposed sensor consists of a central ring with a radius of R_1 that is filled with an analyte is displayed as shown in Fig (1). The purpose of it being in the center is to strengthen the sensitivity to the type of analyte as long as the fundamental mode concentrated in the sensor center. Next, there is a ring of eight air holes of radius R_2 and distance T_1 from the center. These holes are separated by distance Λ_1 and placed at the angles $\theta_1 = \pi/8, 3\pi/8, ..., 15\pi/8$. Next, a ring of eight air holes was made with radii R_3, distance T_2 from the center, and distance Λ_2 from each other. Theses holes are located at the angles $\theta_2 = 0, \pi/4, 2\pi/4, ..., 7\pi/4$. The silica cylinder containing the air and anlyte holes of radius R_4 will be surrounded by sections of gold layer with thickness h. These sections are located at the angles $(2n-1)\pi/8$ to $(2n+1)\pi/8$, $n = 1, 2, 3, 4$. To avoid scattering and reflections, a perfectly matched layer (PML) of thickness $R_5 - R_4$ surrounds the whole composition. Analyte core PCF with noble metal shells: two-dimensional mode characteristics are computed using the COMSOL multiphysics system based on FEM. The design of a typical sensor system configuration is shown in Fig(2), and Table(1) provides the values of the simulation's parameters.

III. SENSOR MATERIALS AND METERS

The sensor is made up of four components: silica, metal, analyte, and air. We assume that the refractive index (RI) of air and analyte remains constant throughout frequency variations if it fluctuates very little in response to physical changes in silica and metal [26]. As such, the following will solely address the properties of metal and silica's RI. The optical properties of a general metallic medium depend on both bound and free electrons [27]. Transitioning from an occupied state below the Fermi level to an unoccupied state in a higher band, interband transitions are intrinsically quantum mechanical phenomena [28]. As it turns out, only a few energy band transitions are involved; these transitions are known to be connected to critical points in the density of states that develop at symmetry points in the Brillouin zone and are commonly called Van Hove singularities [29,30]. Because of the high density of states in these places, interband absorption (and emission) occurs, expanding the observable range from the top of the d-band to levels slightly higher than the Fermi level in the conduction band [31].

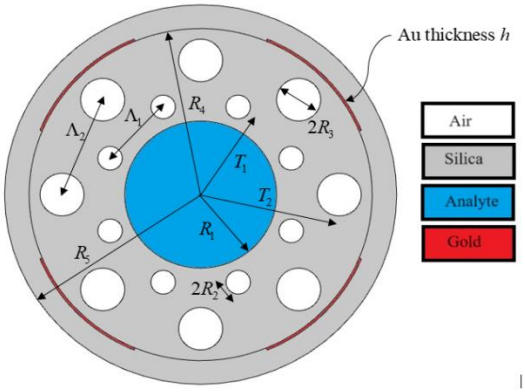

Fig.(1): Cross-section view of the proposed PCF sensor.

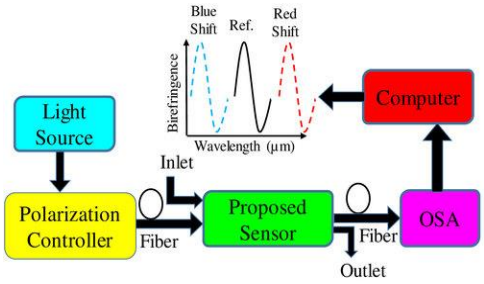

Fig.(2): schematic representation of the usual sensing system configuration.

Table (1): Simulation parameters.

parameter	value(μm)	parameter	value(μm)
R_1	(2.9,3,3.1)	T_1	4
R_2	(0.5,0.6)	T_2	5.66
R_3	(0.7,0.8,0.9)	Λ_1	3.14
R_4	7	Λ_2	4.44
h	0.03, 0.05	R_5	8

Intraband transitions (occurring at low energies) are free-carrier processes. Electrons in the conduction band are regarded free electrons that form an electron gas, and their long-range correlations are interpreted as collective oscillations at the system's plasma frequency w_p [32,33]. Intraband transitions occur when electrons are excited to a higher energy level within the same band, and they contribute to the infrared absorption of free electrons, as described in the Drude model [34]. In this concept, incoming EM radiation with frequencies below is reflected by the electric field of the electrons in the metal screen. Electromagnetic radiation at higher frequencies is transmitted because electrons cannot respond quickly enough to filter it [32]. Thus, the corresponding complex dielectric permittivity incorporates both the Drude component for the intraband effect and the Lorentz term for the interband transition in the form of the Drude-Lorentz model [33]

$$\varepsilon_r(w) = 1 - \frac{w_p^2}{w^2 + i\gamma w} + \sum_i \frac{f_i w_i^2}{w_i^2 - w^2 - i\gamma_i w} \quad (1)$$

where i represents the resonant modes, w_i the resonance frequencies, f_i the weighting coefficients, and w_i the damping effect. It is worth noting that noble metals typically have several interband transitions due to the varied band topologies of bound electrons. The optimal values of typical metals for the Drude-Lorentz model are provided in Table(2). These metals have been widely employed in optoelectronic devices. The measurements of these optical data are heavily influenced by the experimental conditions (in geometrical morphology and manufacturing method), thus the appropriate optical data must be carefully selected.

The sensor's backdrop material was fused silica glass, and the dispersion properties can be calculated using the Sellmier equation [35]

$$n_{sil} = \sqrt{1 + \sum_{j=1}^{3} \frac{A_j \lambda^2}{\lambda^2 - B_j}} \quad (2)$$

where $B_1 = 4.68 \times 10^{-3}\,\mu m^2$, $B_2 = 1.35 \times 10^{-2}\,\mu m^2$, $B_3 = 97.93 \mu m^2$ $A_1 = 0.6961663$, $A_2 = 0.407942$, and $A_3 = 0.8974794$.

Each parameter assesses the performance of a plasmonic sensor, and calculations are carried out using confinement loss for different analyte RI. Confinement loss is a critical parameter for sensitivity measurement, and it may be stated using the following formula [2]

$$\alpha(\frac{dB}{cm}) = 0.868 k_o Im\{n_{eff}\} \times 10^4 \quad (2)$$

where α is the modal loss and $\mathrm{Im}\{n_{eff}\}$ is the imaginary component of effective RI for the fundamental mode. The structural factors used to design the sensor have a significant impact on its performance. For the PCF-SPR sensors, analyte detection happens when there are minute variations in the wavelength of the bio-targets in the surrounding environment. Consequently, one of the most important factors is the spectral sensitivity S_λ, which is described as follows [16]

$$S_\lambda = \frac{\Delta\lambda_{peak}}{\Delta n_a}\left(\frac{nm}{RIU}\right) \quad (4)$$

where $\Delta\lambda_{peak}$ refers to resonance peak difference and Δn_a means the variations in two adjacent RIs of an analyte. Here, $\Delta n_a = 0.01$ is taken in our simulation. Additionally, the resolution of the sensor is important since it indicates the degree to which the sensor can detect changes in analyte RI.

One can compute the sensor resolution using the following relationship [36]

$$R = \frac{\Delta n_a \Delta\lambda_{\min}}{\Delta\lambda_{\text{peak}}}(\text{RIU}) \quad (5)$$

where $\Delta\lambda_{\min} = 0.01nm$ and Δn_a represent the lowest spectral resolution and analyte RI difference, respectively. The sensor length is taken as [32]

$$L = \frac{1}{2\,\mathrm{Im}\{k_{eff}\}} \quad (6)$$

Table(2): Parameter values of gold for the Drude-Lorentz model [34,35].

Parameters	value	Parameters	value
f_o	0.760	γ_3	0.870
γ_d	0.053	w_3	2.969
f_1	0.024	f_4	0.601
$\gamma_1(eV)$	0.241	γ_4	2.494
$w_1(eV)$	0.415	w_4	4.304
f_2	0.010	f_5	4.384
γ_2	0.345	γ_5	2.214
w_2	0.830	w_5	13.32
f_3	0.071		

where $k_{eff} = k_o n_{eff}$ is the effective wavevector and $k_o = 2\pi / \lambda$.

IV. RESULTS AND DISCUSSION

During the simulation, the effects of both gold thickness, the analyte ring radius, the inner air holes radius and the radius of the outer air holes radius are investigated. The following parameters: $h = 50nm$, $R_1 = 3\mu m, R_2 = 0.5\mu m$ $R_3 = 0.9\mu m$ will be taken during the simulation and any changes that occur will be noted in their place throughout the text.

A. Gold Thickness Effect

Fig.(3) displays the relationship of loss with wavelength for several cases of the RI of analyte, where the solid lines indicate the gold thickness *h=50nm* and the discrete-dotted lines represent the gold thickness *h=30nm*. In general, for any RI of analyte, the loss relationship with wavelength achieves a peak. The peak is greatest at $n_a = 1.3$ and decreases with increasing RI of analyte. The resonant wavelength (which achieves the peak) is shifted to the right as RI of analyte increases. The amount of displacement achieved is not the same for all cases. The figure shows that changing the gold thickness did not bring about distinct changes in loss behavior except in the case of $n_a = 1.36$. The resonance frequencies achieved at *h=50nm* differ slightly from those at thickness *h=30nm*.

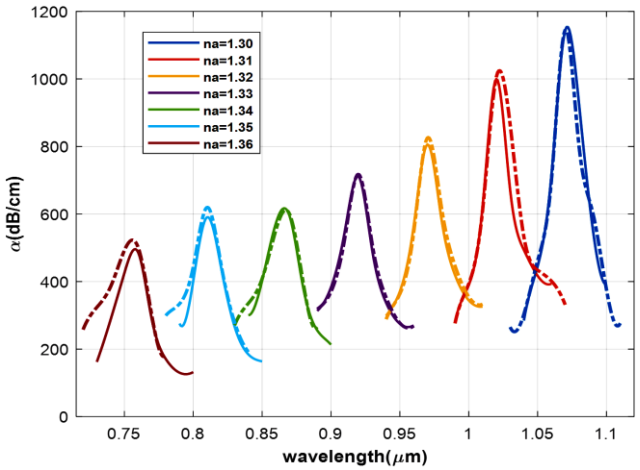

Fig.(3): the loss as a function of wavelength for several analyte RIs, with the continuous and discrete-dotted lines representing $h = 50nm$ and $h = 30nm$, respectively.

Fig.(4) characterizes the spectral sensitivity achieved at each RI of analyte at the thickness of *h=50nm* and *h=30nm*, and we notice that there are slight changes in the sensitivity achieved. In the thickness *h=50nm*, we notice that the sensitivity values in the range (5000-5500)nm/RIU, while at *h=30nm*, the value is in the range (4750-5500)nm/RIU. The sensor resolution attained at each RI of analyte at thicknesses of *h=50nm* and *h=30nm*, is shown in Fig.(5), and we can see that the resolution attained varies slightly. The resolution values at *h=50nm* are found to be in the range $(1.8-2)\times10^{-5}$ RIU, but at *h=30 nm*, they are found to be in the range (1.7-2.1) $\times10^{-5}$ RIU.

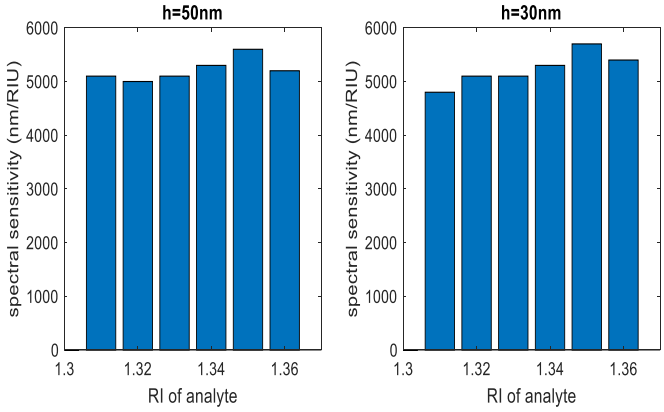

Fig.(4): The spectral sensitivity at *h=50nm* and *h=30nm*.

The sensor resolution versus RI at h=50nm and *h=30nm* is plotted as portrayed in Fig.(5). Histograms are shown for 50 and 30 nm recording a resolution of 2×10^{-5} RIU and exceeds this value for *h=30nm*. Fig.(6) shows the achieved resonance frequency as a function of RI of analyte for the two cases *h=50nm* and *h=30nm*. The illustration suggests that there is a nearly perfect match and that the two situations are linear. The characteristic of linearity is very important in the field of sensors as it can be used to find the resonance frequencies for any refractive index within the range of RI indicated in the figure.

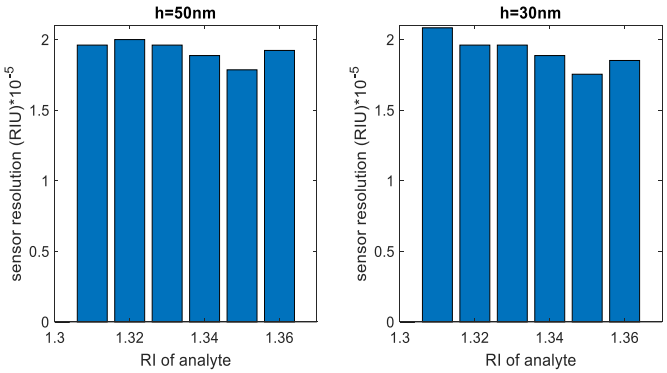

Fig.(5): The sensor resolution at *h=50nm* and *h=30nm*.

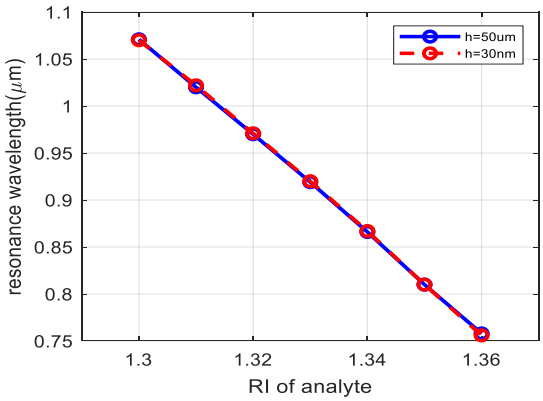

Fig.(6): The wavelength resonance versus RI of analyte.

B. *Analyte Circle Radius Effect*

Three instances of the analyte circle's radius are used in Fig. (7) to illustrate the link between loss and wavelength. The analyte's RI is indicated by the lines' various hues. The graphic shows that all of the curves have been pushed to the right, and that the value of has decreased. In situations $R_1 = 3.1\mu m, 2.9\mu m$, the curves are slightly deformed, while in case $R_1 = 3\mu m$, they are regular. The peaks in this case are as high as possible and consistently drop as the analyte's RI increases. Therefore, it would be appropriate for the design to use the value $R_1 = 3.1\mu m$. The corresponding spectral sensitivity of each RI of analyte to different cases of R_1 is sketched in Fig(8). We notice from the figure that the spectral sensitivity is more regular only in case $R_1 = 3\mu m$, and it varies greatly in case $R_1 = 3.1\mu m$, and more so in case $R_1 = 2.9\mu m$. Fig.(9) demonstrates the sensor resolution of each RI of analyte to different cases of R_1. We notice from the figure that the sensor resolution is within (1.4-2.1) $\times10^{-5}$ RIU range in case $R_1 = 3.1\mu m$ within (1.8-2) $\times10^{-5}$ RIU range in case $R_1 = 3\mu m$ and within (1.3-2.7) $\times10^{-5}$ range

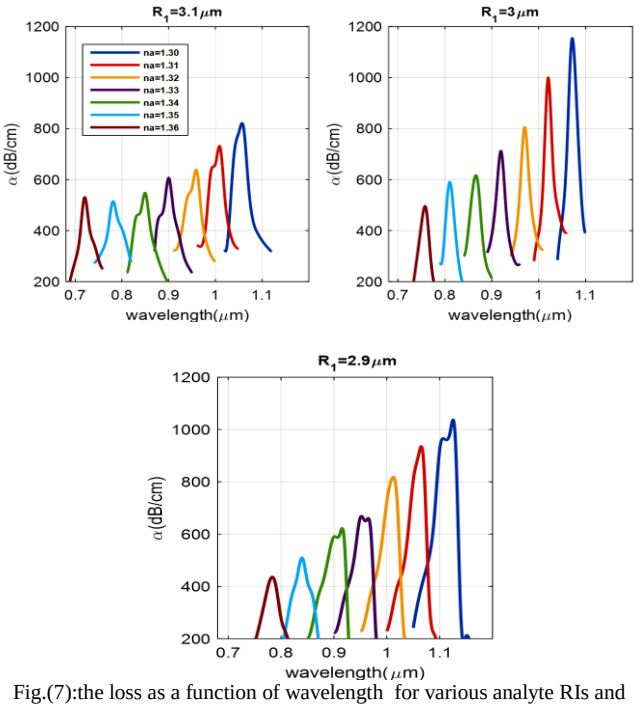

Fig.(7):the loss as a function of wavelength for various analyte RIs and R_1 values.

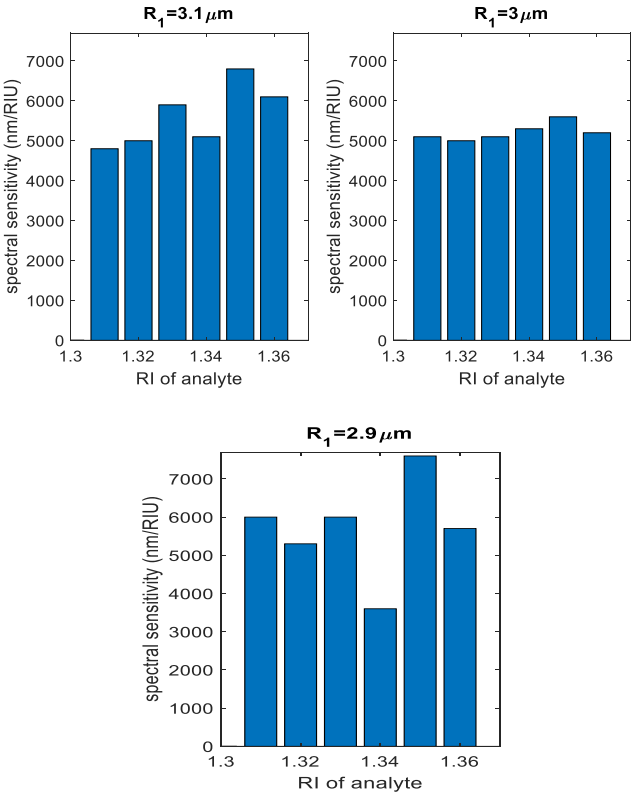

Fig.(8): The spectral sensitivity for many values of R_1.

RIU in case $R_1 = 2.9\mu m$. . The fluctuation of sensor resolution is only acceptable for case $R_1 = 3\mu m$, and for the rest of the case, it is unacceptable because it gives divergent values for different RI of analyte. Fig.(10) indicates the corresponding resonant wavelength for RI of analyte for different values of R_1. It is clearly evident from the figure that the regular linear characteristic is only achieved for case $R_1 = 3\mu m$, and it deviates from the linearity property in case $R_1 = 3.1\mu m$, and deviates more for case $R_1 = 2.9\mu m$. This confirms what was mentioned above about spectral sensitivity and sensor resolution.

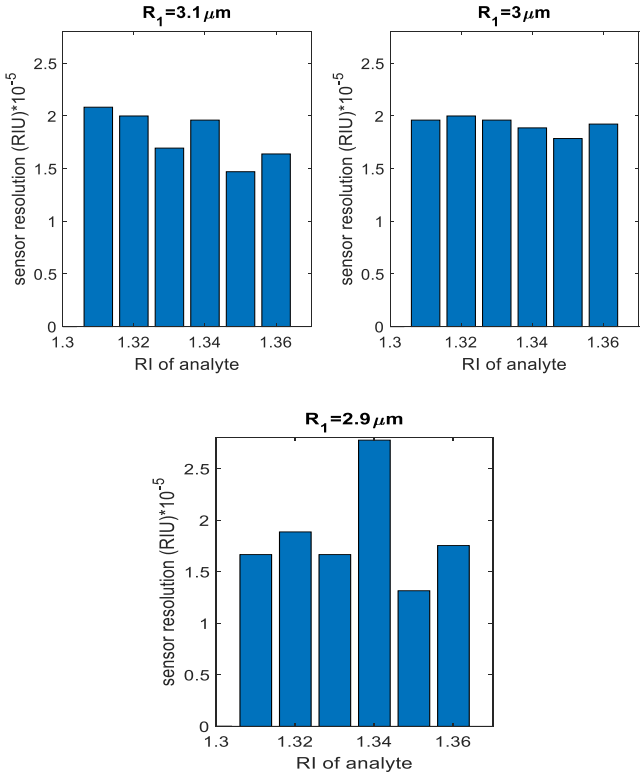

Fig.(9): The sensor resolution for many values of R_1.

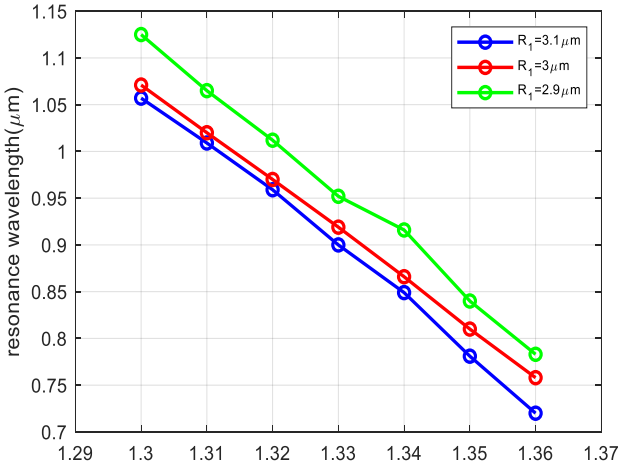

Fig.(10): The wavelength resonance as a function of RI of analyte for different R_1.

C. *Outer Air Circle Radius Effect*

Fig.(11) depicts the loss against of wavelength for different values of RI of analyte using different radii of the air holes in the outer ring. We note that decreasing the value of R_3 will cause shifts towards the right for all curves, the

highest peaks will occur at $R_3 = 0.8\mu m$ and the lowest peaks that will be distorted at $R_3 = 0.7\mu m$. Regularity of decreasing peaks occurs in a systematic manner only in case $R_3 = 0.9\mu m$. Whereas the decrease of the peaks occurs with the increase in the RI of analyte.

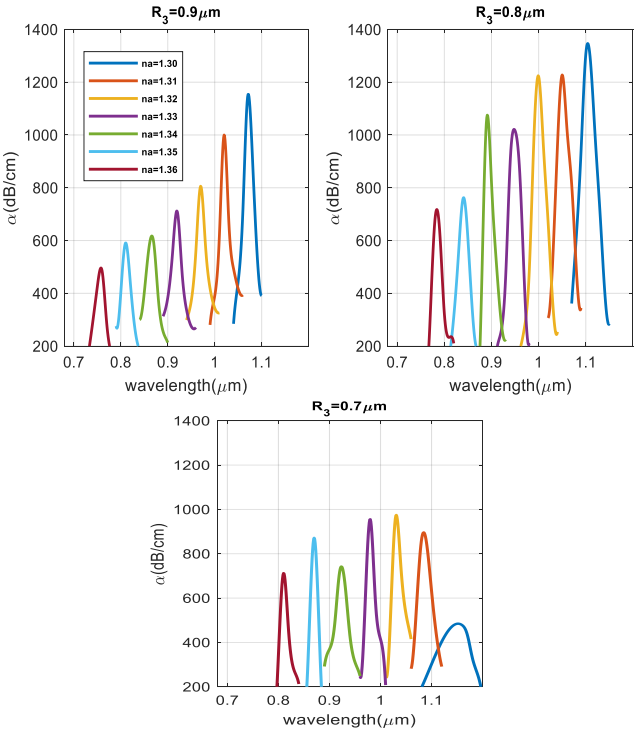

Fig.(11):the loss as a function of wavelength for various analyte RIs and R_3 values.

Fig.(12) represents the corresponding spectral sensitivity of each RI of the analyte for different values of R_3. It is clear from the figure that the best quasi-stable sensitivity occurs at $R_3 = 0.9\mu m$, which values are within the range (5000-5500)nm/RIU. The rest of the R_3 cases give higher sensitivity in certain cases, but it varies greatly for different RI of analyte cases. The same words above apply to Fig.(13), which represents the sensor resolution for different cases of R_3, where small values can be achieved in cases $R_3 = 0.7\mu m, 0.8\mu m$, but they vary greatly, and the best case that gives acceptable and close values is $R_3 = 0.9\mu m$. Fig.(14) displays the resonance frequency corresponding to different of RI of analyte at several cases of R_3. We note that the first two cases $R_3 = 0.9\mu m, 0.8\mu m$ achieve near-perfect linearity, and the third case $R_3 = 0.7\mu m$ deviates slightly from the linearity property. According to what was mentioned above, we can confirm that the best suitable condition for work is $R_3 = 0.9\mu m$.

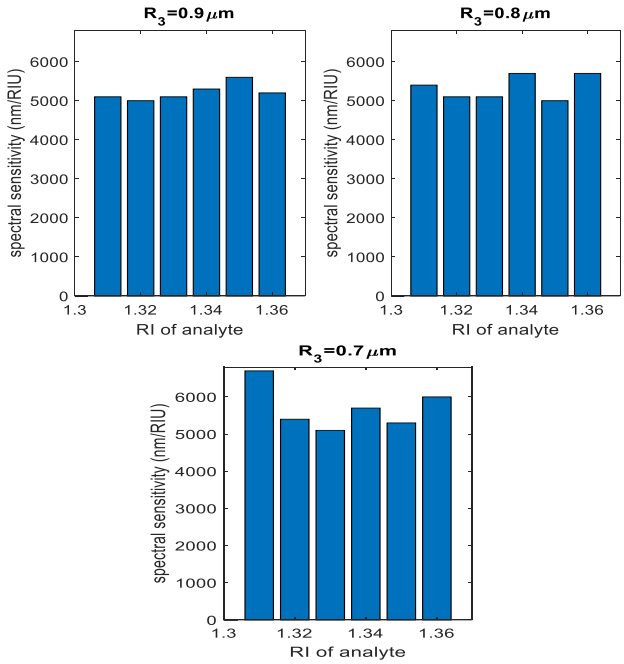

Fig.(12): The spectral sensitivity for many values of R_3.

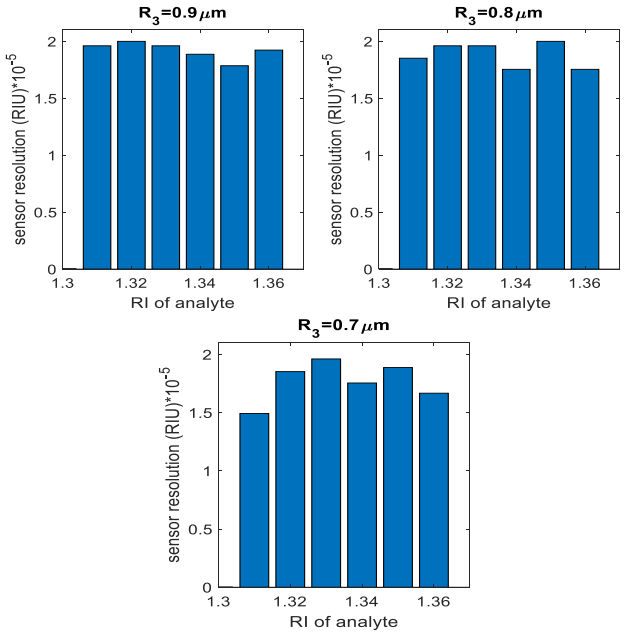

Fig.(13): The sensor resolution for many values of R_3.

D. *Inner Air Circle Radius Effect*

Fig.(15) represents the loss versus the wavelength for different values of RI of analyte using two radii of the air holes in the inner ring. We note that the value $R_2 = 0.5\mu m$ makes the loss curves regularly decreasing with the change in RI of analyte. But the value $R_2 = 0.6\mu m$ destroys the regularity and achieves small loss values. The curves are not shifted due to changing the value of R_2. Fig.(16) represents the spectral sensitivity achieved for different RI of analyte using the $R_2 = 0.5\mu m, 0.6\mu m$ values. We note that the first case has close values for all RI of analyte, but the second case may achieve higher sensitivity, but the values are not close. The same behavior applies to Fig,(17), which

concerns sensor resolution. The resonance frequency corresponding to different of RI of analyte at two cases of R_2 is plotted as drawn in Fig.(18). We note that the first case $R_2 = 0.5\mu m$ achieve near-perfect linearity, and the second case $R_2 = 0.6\mu m$ deviates from the linearity property.

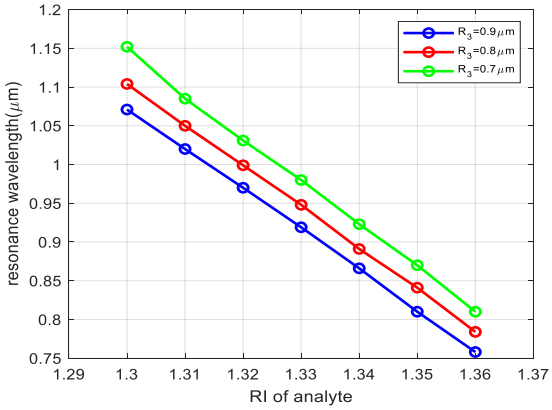

Fig.(14): The wavelength resonance as a function of RI of analyte for different R_3.

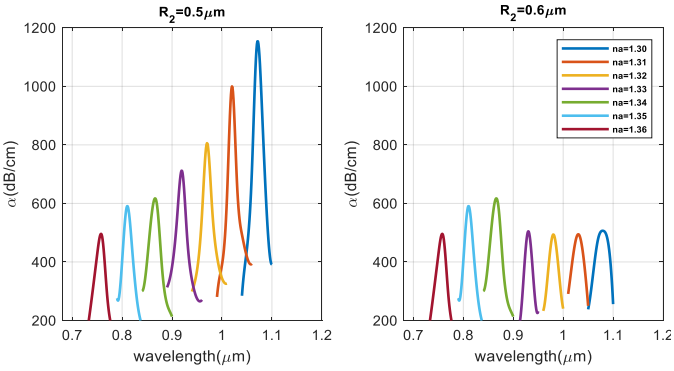

Fig.(15): The loss as functions of wavelength for many RI of analyte, for two values of R_2.

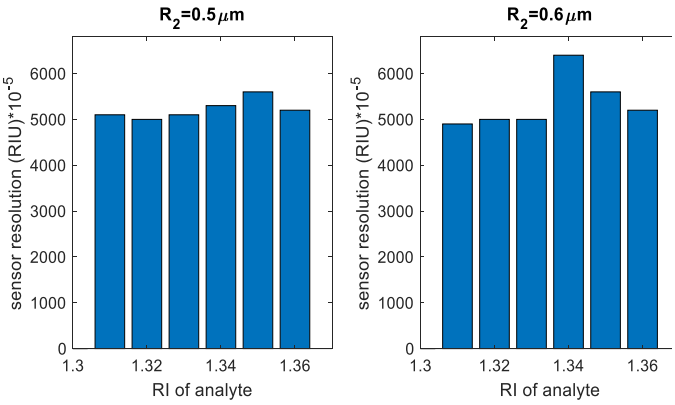

Fig.(16): The spectral sensitivity for many value of R_2.

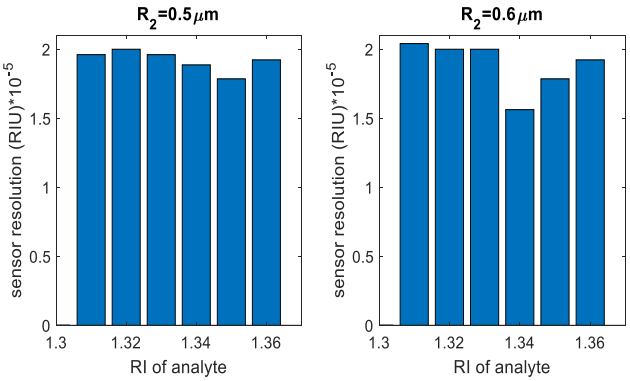

Fig.(17): The sensor resolution for two values of R_2.

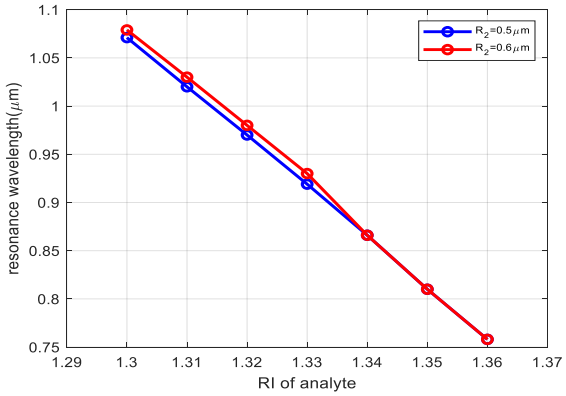

Fig.(18): The wavelength resonance as a function of RI of the analyte for different R_2.

E. Sensor Length

Fig.(19) represents the relationship of the sensor length against the RI of analyte for a selected cases. The sensor length is chosen to satisfy all cases of RI of analyte. It is clear from the figure that large changes in the sensor length are caused by a small change in the simulation values. Table(3) summarizes a comparison with many scientific results.

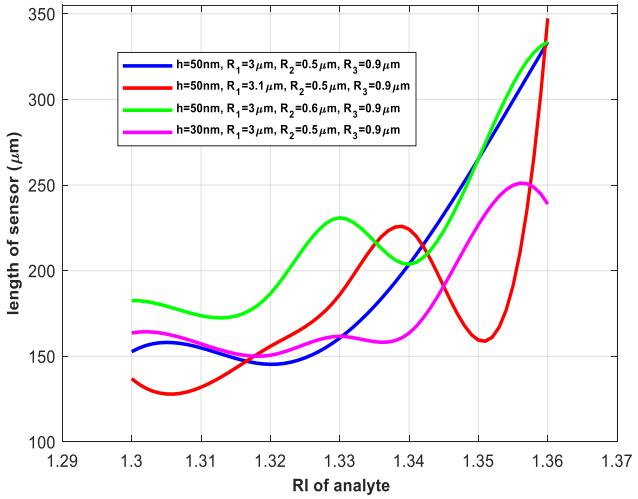

Fig.(19): Sensor length as a function of RI of analyte for selected cases.

Table(3): Comparative study of the performance with existing PCFs as RI sensor.

Ref.	Sensitivity (nm/RIU)	Sensor resolution (RIU)	Range of RI of analyte
[11]	2300-4600	2×10^{-5} -7×10^{-5}	1.33–1.36
[16]	1000-10000	5×10^{-6} -1×10^{-4}	1.33-1.42
[25]	3000-9000	4.55×10^{-6} -8×10^{-5}	1.33-1.38
[31]	2000-8000	8.33×10^{-6}	1.33-1.40
present sensor	5000-7500	2×10^{-5} -3×10^{-5}	1.30-1.36

V. CONCLUSIONS

In conclusion, we found that changing the thickness of the gold layer did not show distinct changes in the properties of the sensor. The radius of the analyte circle is very influential in the sensitivity and sensor resolution achieved, where $R_1 = 3\mu m$ achieves the best convergent values for all RI of analyte. The radii of the air holes in the inner and outer ring is also an effective factor in obtaining close values of sensitivity and sensor resolution, where $R_2 = 0.5\mu m$, $R_3 = 0.9\mu m$ achieve the best results. The obtained sensitivity and resolution rates are listed in sequence as 5000nm/RIU and 2×10^{-5} RIU. For the identical settings as earlier, the best linearity in the resonance wavelength relationship with the RI of analyte was obtained. When the RI ranges from 1.30 to 1.36, this linear characteristic allows the sensor to identify the unknown analyte. In general, sensor parameters testing revealed that $h = 50nm$, $R_1 = 3\mu m$, $R_2 = 0.6\mu m$ and $R_3 = 0.9\mu m$ that yield the best results.

CONFLICT OF INTEREST

Authors declare that they have no conflict of interest.

REFERENCES

[1] V. Kaur and S. Singh, "Design approach of solid-core photonic crystal fiber sensor with sensing ring for blood component detection", *Journal of Nanophotonics* 13(2), 026011, 2019.

[2] M. Salman, H. Muhammad and H. Yasser. "Effects of holes radius on plasmonic photonic crystal fiber sensor with internal gold layer", *Periodicals of Engineering and Natural Sciences*, Vol. 8, pp.1288-1296, 2020.

[3] A. Talib and H. Yasser. "Maximizing spectral sensitivity of plasmonic photonic crystal fiber sensor", *Optik - International Journal for Light and Electron Optics* 249, 168228, 2022.

[4] O. Zhernovaya, O. Sydoruk, V. Tuchin and A. Douplik, "The refractive index of human hemoglobin in the visible range", *Physics in medicine and biology*, 56, 4013–4021, 2011.

[5] B. Li, T. Cheng, J. Chen, and X. Yan, "Graphene-enhanced surface plasmon resonance liquid refractive index sensor based on photonic crystal fiber," *Sensors*, vol. 19, p. 3666, 2019.

[6] S. Mostufa, A. Paul and K. Chakrabarti, "Detection of hemoglobin in blood and urine glucose level samples using a graphene-coated SPR based biosensor", *OSA Continuum*, Vol.4, No.8, 2021.

[7] R. Hani, B. Mahdi, and A. Mohammed, "Photonic crystal fiber sensor for blood with different concentration of zinc", *Materials Science Forum* Vol.1002, 2020.

[8] A. Bulbul, R. Jibon, S. Biswas, S. Pasha and Md. Sayeed, "Photonic crystal fiber-based blood components detection in THz regime: Design and simulation", *Sensors International*, Vo.l2, 100081, 2021.

[9] E. Lazareva and V. Tuchina, "Measurement of refractive index of hemoglobin in the visible/NIR spectral range", *Journal of Biomedical Optics* 23(3), 035004, 2018.

[10] S. Maier, "Plasmonics: fundamentals and applications", Springer Science and Business Media. 2007, ch.2-3, pp.5-35.

[11] R. Otupiri, E. Akowuah, and S. Haxha , "Multi-channel SPR biosensor based on PCF for multi-analyte sensing applications", *Optics express* 15716, 2015.

[12] G. Igorevich, D. Petr, C. Olga, and F. Vyacheslav, and K. Mikhail, "Study of glucose concentration influence on blood optical properties in THz frequency range", *Nanosystems: physics, chemistry, mathematics*, 9 (3), 2018.

[13] M. Islam, A. Iftekher, K. Hasan, J. Nayen, S. Islam, Md. Khan, J. Chowdhury, F. Mehjabin, M. Islam, and Md. Islam, "Design and analysis of a biochemical sensor based on surface plasmon resonance with ultra-high sensitivity", *Plasmonics* 16(9), 2021.

[14] J. Lu, Y. Li, Y. Han, Y. Liu, and J. Gao, , 2018, "D-shaped photonic crystal fiber plasmonic refractive index sensor based on gold grating," *Applied optics*, vol. 57, pp. 5268-5272.

[15] M. Elblbesy, "The refractive index of human blood measured at the visible spectral region by single-fiber reflectance spectroscopy", *Biophysics*, 8(1): 57–65, 2020.

[16] E. Misto, A. Supriyadi, L. Rohman, and B. Cahyono, "Analyses of concentration and wavelength dependent refractive index of sugar solution using Sellmeier equation", *Journal of Physics: Conference Series*, Vol. 1825, No. 1, 2021.

[17] A. Belay and G. Assefa, "Concentration, wavelength and temperature dependent refractive index of sugar solutions and methods of determination contents of sugar in soft drink beverages using laser lights", *J Laser Opt Photonics* 5:2, 2018.

[18] N. Ayyanar1, P. Kuppusamy, G. Raja, D. Vigneswaran, and A. Aly, "Tricore photonic crystal fiber based refractive index sensor for glucose detection", *IET Optoelectronics* 13(3), 2018.

[19] F. Zha, J. Li, P. Sun, and H. Ma, "Highly sensitive selectively coated D-shape photonic crystal fibers for surface plasmon resonance sensing," *Physics Letters A*, vol. 383, pp. 1825-1830, 2019.

[20] M. Hasan, M. Rahman, K. Ahmed and M. Rana, "Design and analysis of a highly sensitive plasmonic photonic crystal fiber biosensor", *IEEE Access*, 8, 199202–199213, 2020.

[21] F. Zhenkai, "Surface plasmon resonance refractive index sensor based on photonic crystal fiber covering

nano-ring gold film", Optical Fiber Technology 50: 194-199, 2019.
sensor using the lower birefringence peak method", *OSA Continuum*. Vol.2, No.5, 2019.
[22] G. An, S. Li, Y. An, H. Wang, and X. Zhang "Glucose sensor realized with photonic crystal fiber-based Sagnac Interferometer", *Optics Communications* 405, 143–146, 2017.
[23] A. Borji, Fz. Borji, and A. Jourani. "A new method for the determination of sucrose concentration in a pure and impure system: spectrophotometric method", *International Journal of Analytical Chemistry*, Vol.2017, 2017.
[24] A. Rakic, A. Djuris, J. Elazar, and M. Majewski, "Optical properties of metallic films for vertical-cavity optoelectronic devices", *Applied optics*, Vol. 37, No. 22, 1998.
[25] M. Mahfuz, Md. Hasan, M. Momota, and S. Akter, "Asymmetrical photonic crystal fiber based plasmonic refractive index sensor," *Sensors*, vol. 19, p. 3794, 2019.
[26] X. Yang, Y. Lu, M. Wang and J. Yao, "A photonic crystal fiber glucose sensor filled with silver nanowires." *Optics Communications* 359, pp.279-284, 2016.
[27] X. Zhang, S. Feng, J. Zhang, T. Zhai, H. Liu, and Z. Pang,"Sensors based on plasmonic photonic coupling in metallic photonic crystals," *Sensors*, vol. 12, pp. 12082-12097, 2012.
[28] M. Mahfuz, M. Hossain, E. Haque, N. Hai, Y. Namihira, and F. Ahmed, "A bimetallic-coated, low propagation loss, photonic crystal fiber based plasmonic refractive index sensor," *Sensors*, vol. 19, p. 3794, 2019.
[29]J. Dash and R. Jha, 2015, "On the performance of graphene-based D-shaped photonic crystal fibre biosensor using surface plasmon resonance," *Plasmonics*, vol. 10, pp. 1123-1131.
[30] Y. Lu, C. Hao, B.. Wu, X. Huang, W. Wen, X. Fu, *et al.* "Grapefruit fiber filled with silver nanowires surface plasmon resonance sensor in aqueous environments," *Sensors*, vol. 12, pp. 12016-12025, 2012.
[31] C. Wang, X. Zhang, H. Li, and Z. Liu, "Highly sensitive plasmonic photonic crystal fiber biosensor for label-free detection," *Optics Express*, 27(20), 28533-28544, 2019.
[32] H. Ali, H. Ammar, and H. Yasser, "Metal type effect on plasmonic fiber properties," *IOP Materials Science and Engineering* 928, 2020.
[33] K. Kolwas and A. Derkachova, "Impact of the interband transitions in gold and silver on the dynamics of propagating and localized surface plasmons," *Nanomaterials*, 10, 1411, 2020.
[34] M. Dresselhaus, "Solid-state physics," Lecture Notes, Part II; Optical Properties of Solids; Massachusetts Institute of Technology: Cambridge, MA, USA, Volume 17, 2001.
[35] G. Agrawal, "Nonlinear fiber optics", 5th edition, Academic Press, 2012, ch.2, pp.6-7.
[36] Y. Zhang, J. Liu, Y. Lu, S. Guo, X. Xiao, and Z. Yang, "Recent progress on plasmonic photonic crystal fiber sensors: mechanisms, materials, and applications," *Sensors*, 21(10), 3421, 2021.